Macromolecules

pubs.acs.org/Macromolecules Article

# Epitaxial Assembly of Nanoparticles in a Diblock Copolymer Matrix: Precise Organization of Individual Nanoparticles into Regular Arrays

Jiabin Gu, Runrong Zhang, Liangshun Zhang,* and Jiaping Lin*

Cite This: *Macromolecules* 2021, 54, 2561−2573 Read Online

ACCESS | Metrics & More | Article Recommendations | Supporting Information

**ABSTRACT:** Precise organization of nanoparticles (NPs) into regularly well-defined arrays represents a continuing challenge in the development of high-performance metamaterials. Herein, zone-annealed diblock copolymers provide an effective medium for construction of periodically well-ordered arrays of NPs within mechanically enhanced nanocomposites. By integrating the dynamic self-consistent field theory for diblock copolymers and molecular dynamics for NPs, it is revealed that the emergence of response layers of asymmetric diblock copolymers induces the epitaxial assembly of NPs during the processing of hot zone annealing. In particular, the ability to kinetically control the assembly pathway of NPs enables them to be organized into hexagonally packed, defect-free arrays, with essentially the individual NP in a unit cell. Our simulations also show that the moving speed of annealing fronts and the concentration and radius of NPs all play important roles in engineering both the spatial arrangement and organization of NPs in a diblock copolymer matrix. Furthermore, the information from the simulations of diblock copolymer/NP mixtures is used to deduce mechanical responses of polymeric nanocomposites by the lattice spring model. The results reveal that the spatial arrangement and organization of NPs in the diblock copolymer matrix provide additional reinforcing elements to enhance the strength of structural materials. Merging the self-assembly of nanocomposites with the zone annealing processing can provide a means of kinetically controlling the assembly pathway for the achievement of regularly well-ordered arrays of polymer-embedded NPs with structural and optoelectronic functionalities.

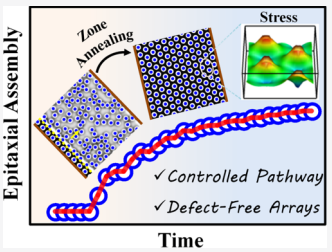


## 1. INTRODUCTION

Precise organization of functional nanoparticles (NPs) into addressable, regular arrays is a critical prerequisite for development of next-generation devices and utilization of optoelectronic metamaterials.[1−4] Conventional strategies of utilizing electron-beam lithography or photolithography have been proposed to build upon the regular arrays of particles or colloids with larger feature sizes.[5] As geometrical features of NPs are pushed toward deep sub-100 nm scales, lithographic strategies are costly and time-consuming for fabrication of highly regular arrays of NPs due to the resolution limits of conventional lithography equipment. Nevertheless, regularly well-ordered arrays of NPs offer significant opportunities for improving the collective electronic, optical, and magnetic properties of nanodevices.[6−8] For instance, periodic arrays of plasmonic NPs could extremely enhance Fano-like resonances of optically active nanocomposites.[9,10] Hence, it is particularly urgent to propose facile and effective strategies for tailoring the spatial arrangement of NPs and achieving their well-ordered arrays without arrested defects.

Utilization of templates or scaffolds (*e.g.*, DNA, functionalized polymers, and diblock copolymers) to direct the ordering and local environment of NPs is ideal for scalable fabrication of regular arrays of NPs.[11−13] Among these, diblock copolymers can spontaneously assemble into a diversity of periodically well-defined nanostructures such as hexagonally close-packed cylinders and lamellae,[14−16] which are used as scaffolds to host NPs within thermodynamically compatible nanodomains. Such coassembly of diblock copolymer/NP mixtures offers a viable route to prepare hybrid materials integrating unique functionalities of fillers and matrices.[17−23] However, because of the impractically slow self-assembly kinetics and long-lived defects in the ordering process, the diblock copolymers self-assemble into poorly ordered nanostructures, whose grain sizes have several disparate periodicities. These phenomena result in a grand challenge for efficient manufacturing of regularly defect-free arrays of NPs *via* the coassembly strategy of diblock copolymer/NP mixtures.

To address the above challenge, both experimental and theoretical researchers have devised a variety of methods (*e.g.*, chemical epitaxy,[24] topographical epitaxy,[25] and utilization of external fields like the shear flow and temperature gradient[26−28]) to drive the self-assembly of pure diblock copolymers into defect-free nanostructures. In particular, on the basis of the nonuniform temperature field, the zone-annealing method originally proposed in the metallurgy and semiconductor industry imposes a directional bias on the growth of self-assembled nanostructures within a movable

Received: January 5, 2021
Revised: February 9, 2021
Published: February 17, 2021







https://dx.doi.org/10.1021/acs.macromol.1c00028
*Macromolecules* 2021, 54, 2561−2573

narrow region,[29,30] resulting in rapid and continuous fabrication of highly ordered patterns of diblock copolymers. Depending upon the temperature in the narrow region of experimental samples, the method can be categorized as cold zone annealing (CZA) and hot zone annealing (HZA). In the case of CZA,[30,31] where the upper-bound temperature is typically around the order−disorder transition temperature ($T_{ODT}$), long-lived defects of diblock copolymers are annihilated in a short annealing time, and they gradually evolve into highly ordered nanostructures. However, the distinct ordering mechanism of diblock copolymers subject to HZA emerges in virtue of the temperature above the $T_{ODT}$.[32,33] The ordering and alignment of disordered diblock copolymers located in the narrow region are triggered by the directed assembly of formed nanostructures, which were also demonstrated by the theoretical simulations.[34−37] The ordering process of diblock copolymers subject to HZA is conceptually analogous to the directional solidification and epitaxy of crystalline materials.[38−40] Thus, the highly ordered nanostructures of zone-annealed diblock copolymers can provide an effective medium for spatially organizing the inorganic NPs within the organic matrix.

In our recent work, an integrated dynamic self-consistent field theory (DSCFT) and molecular dynamics (MD) method was developed to probe into the structural evolution of symmetric diblock copolymer/NP mixtures.[41] We introduced a narrow region with the Flory−Huggins interaction parameter (inversely proportional to the temperature in experiments) around the order−disorder transition value, corresponding to the case of CZA. As noted above, owing to the ordering mechanism of defect annihilation, the CZA method facilitates the nanocomposites to rearrange from defective patterns to well-defined lamellae in a limited time and drives the NPs to locate in energetically favorable nanodomains. It should be particularly pointed out that the regularly well-ordered arrays of NPs cannot be achieved in the polymer matrix subject to CZA. In turn, HZA with epitaxial characteristics provides unique opportunities to kinetically tune the self-assembly pathway of diblock copolymers and potentially to program the spatial arrangement and organization of NPs. Nevertheless, little is known about the ordering mechanics and influence of HZA on the structural formation of nanocomposites and the organization of NPs in a diblock copolymer matrix.

Another motivation for construction of regularly well-ordered arrays of NPs arises from a significant demand to boost the light-weight mechanical reinforcement of flexible nanocomposites.[42−48] For this reason, we also elucidate how the spatial arrangement and organization of NPs within the matrix impact the mechanical responses of polymeric nanocomposites. Ultimately, the polymeric nanocomposites used for optoelectronic applications not only should show extremely enhanced optical activity but also must be mechanically robust. Thereby, it is a critical issue to be addressed before further application of inorganic NPs for novel nanocomposites with well-ordered nanostructures and desirable attributes.

In this contribution, a multiscale modeling is proposed to pinpoint the conditions of HZA for realization of regularly well-ordered nanostructures as well as correlate the self-assembled nanostructures of nanocomposites with their mechanical properties. Herein, we first utilize the integrated DSCFT/MD simulations in larger boxes to examine the structural evolution of nanocomposites in the presence of HZA. As we show below, HZA provides a means of kinetically controlling the self-assembly pathway of diblock copolymers and thereby induces precise organization of NPs into regular arrays, which cannot be achieved by CZA. Subsequently, the output patterns of DSCFT/MD simulations serve as the input configurations of the lattice spring model (LSM),[49−51] which allows us to determine the stress/strain distributions and global Young's modulus of polymeric nanocomposites. The study described herein will enhance our understanding of how regulation of self-assembly pathways of hybrid systems can be harnessed to control hierarchical nanostructures of nanocomposites and spatial regularities of distinct components, which contribute different functionalities to yield mechanically integrated, multifunctional metamaterials.

## 2. THEORETICAL MODEL AND COMPUTATIONAL METHOD

In this section, a multiscale modeling is proposed to probe into the relationship between self-assembled nanostructures and mechanical properties of nanocomposites. In particular, the integrated DSCFT/MD method is used to describe the structural evolution of nanocomposites and uncover the ordering mechanisms. The self-assembled nanostructures obtained from the DSCFT/MD simulations serve as input configurations of the LSM, which is applied to determine the mechanical properties of resultant materials. Consequently, the combination of these methods allows us to relate the nanoscopic structures and macroscopic properties of nanocomposites.

**2.1. Integrated DSCFT/MD Method of Nanocomposites.** The DSCFT for polymeric fluids and the MD for nanoscopic particles are integrated to investigate self-assembly behaviors of zone-annealed nanocomposites in volume $V$, which consist of $n$ chains of AB diblock copolymers and $n_P$ NPs (designated as P below). The diblock copolymers with volume fraction $f_A$ of A blocks are modeled by Gaussian chains. The basic length unit is denoted by ideal gyration radius $R_g$ of polymer chains with length $N$. The $i$-th NP with radius $R_P$ at position $\mathbf{r}_i$ is denoted by a hyperbolic tangent function given by $h(\mathbf{r}, \mathbf{r}_i) = (1 - \tanh[(|\mathbf{r} - \mathbf{r}_i| - R_P)/\lambda])/2$,[52] where $\lambda$ is the thickness of the interface between NPs and polymeric fluids. Such a smooth profile for the NPs has better convergence results and also implicitly takes into account ligands attached on their surfaces.[53] The local density field of NPs is given by $\varphi_P(\mathbf{r}) = \sum_{i=1}^{n_P} h(\mathbf{r}, \mathbf{r}_i)$. The concentration of NPs in the nanocomposites is defined as $c_P = V_P/V$, where $V_P = \int d\mathbf{r}\varphi_P$ describes the total volume of NPs.

On the basis of field-theoretic frameworks of polymers, the dimensionless free energy functional $F$ of nanocomposites is taken to be[54]

$$F = -n(1 - c_P)\ln\frac{Q_{AB}}{V(1 - c_P)} + \frac{n}{V}\int d\mathbf{r}\left\{-\sum_M \omega_M\varphi_M + \sum_{KL}\chi_{KL}N\varphi_K\varphi_L + \frac{1}{2}\kappa_H\left(\sum_K \varphi_K - 1\right)^2\right\} + \sum_{i=1}^{n_P-1}\sum_{j>i}^{n_P}\int d\mathbf{r}h(\mathbf{r}, \mathbf{r}_i)\int d\mathbf{r}'h(\mathbf{r}', \mathbf{r}_j)u(|\mathbf{r} - \mathbf{r}'|) \quad (1)$$


https://dx.doi.org/10.1021/acs.macromol.1c00028
Macromolecules 2021, 54, 2561−2573

where includes contributions from polymeric fluids, coupling between polymers and particles as well as inter-particles. $\chi_{KL}N$ (K, L = A, B, and P) signifies sets of Flory−Huggins interaction parameters between distinct components. $\varphi_K$ is the local density field of the K-type component. External potential fields $\omega_M$ (M = A and B) are bijectively related to given density fields by the functional $\varphi_M[\omega_M]$. $Q_{AB}$ is the normalized partition function of a single chain. The Helfand-type coefficient $\kappa_H$ enforces finite compressibility to the system. The purely repulsive Lennard-Jones potential $u(|\mathbf{r} - \mathbf{r}'|)$ is used to prevent the overlay of NPs.

In the DSCFT method, temporal evolution of local density fields $\varphi_K$ (K = A and B) of diblock copolymers is assumed to obey the Cahn−Hilliard-like equation in space $\mathbf{r}$ and time $t$[55,56]

$$\frac{\partial \varphi_K(\mathbf{r}, t)}{\partial t} = M_K \nabla \cdot \varphi_K(\mathbf{r})[(\mathbf{I} - \mathbf{n}_S \otimes \mathbf{n}_S) \cdot \nabla \mu_K(\mathbf{r})] + \eta_K(\mathbf{r}, t) \quad (2)$$

where $M_K$ denotes the mobility coefficient of the K-type component, $\mathbf{I}$ is the unit tensor, $\mathbf{n}_S \equiv -\nabla\varphi_P/|\nabla\varphi_P|$ is the local unit vector perpendicular to the surface of the particles, $\mu_K(\mathbf{r}) \equiv \delta F/\delta\varphi_K(\mathbf{r})$ is the chemical potential derived from the free energy functional eq 1, and $\eta_K$ is the thermal noise. The operator $\mathbf{I} - \mathbf{n}_S \otimes \mathbf{n}_S$ is introduced to make the NPs "hard" with respect to the polymeric fluids, that is, the copolymer molecules cannot penetrate into the regions occupied by the NPs.

In the MD method, motion of the $i$-th NP with mass $m_i$ is governed by the following Newton's equations[57]

$$\frac{d\mathbf{r}_i}{dt} = \mathbf{v}_i \quad (3)$$

$$m_i \frac{d\mathbf{v}_i}{dt} = \int d\mathbf{r} f_i(\mathbf{r}) \quad (4)$$

Herein, $\mathbf{v}_i$ is the velocity of the $i$-th NP and $f_i(\mathbf{r})$ designates the body force, expressed as

$$f_i(\mathbf{r}) = h(\mathbf{r}, \mathbf{r}_i)(-\nabla\mu_i(\mathbf{r}) - \mathbf{v}_i/M_P - \nabla\theta_i) \quad (5)$$

where $\mu_i(\mathbf{r}) \equiv \delta F/\delta h(\mathbf{r}, \mathbf{r}_i)$ is the chemical potential of the $i$-th NP derived from eq 1, $\theta_i$ labels the random variable, and $M_P$ is the mobility coefficient of NPs.

The zone-annealing model of diblock copolymer/NP mixtures is presented in Figure 1a. In the system of nanocomposites, the Flory−Huggins interaction parameters $\chi_{KL}N$ are varied spatiotemporally and used to divide the system into three regions. In region I, the interaction parameters have the maximum values $(\chi_{KL}N)_{max}$, which are higher than the order−disorder transition value $(\chi_{AB}N)_{ODT}$ of diblock copolymers without fillers. In region III, the interaction parameters have the minimum values $(\chi_{KL}N)_{min}$, and $(\chi_{KL}N)_{min} < (\chi_{AB}N)_{ODT}$. In region II, $\chi_{KL}(\mathbf{r}, t)N$ are uniform in the $y$ direction, and the connection between $(\chi_{KL}N)_{max}$ and $(\chi_{KL}N)_{min}$ in the $x$ direction satisfies the hyperbolic tangent function. In Figure 1a, the annealing front marked by the dashed line satisfies the condition $\chi_{KL}(\mathbf{r}, t)N = (\chi_{AB}N)_{ODT}$ and is moved along the $x$ direction at a constant speed $v$. Experimentally, this situation can be achieved by utilizing the spatiotemporal change of the temperature field, which is inversely proportional to the Flory−Huggins interaction parameters. The model under the parameter setting of $(\chi_{KL}N)_{min} \ll (\chi_{AB}N)_{ODT}$ corresponds to the case of HZA.

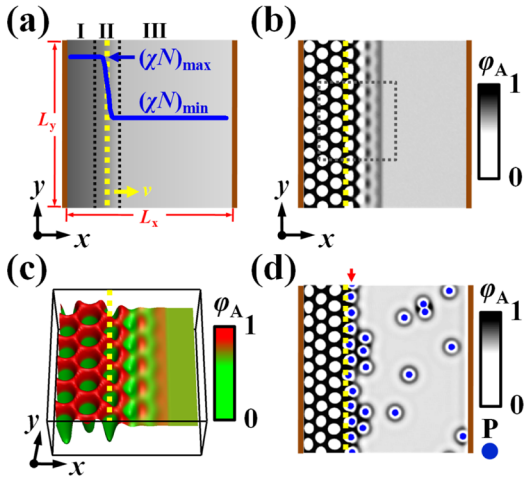


**Figure 1.** (a) Schematic illustration of epitaxial self-assembly of polymeric nanocomposites. Inset shows the profile of the Flory−Huggins interaction parameter $\chi N$ along the $x$ direction, which is used to distinguish the system into regions I, II, and III. The annealing front highlighted by the yellow dashed line is moved with a constant speed $v$. The neutral walls are indicated by the brown color. (b) Self-assembled nanostructures of diblock copolymers in the presence of stationary fronts at a late time. (c) Three-dimensional height map of the density field of A-block enclosed by the dashed box in the panel (b). (d) Self-assembled nanostructures of polymeric nanocomposites subject to stationary fronts at a late time. The arrow highlights the monolayer of NPs. The A- and B-rich domains are represented by dark and bright colors, respectively. The blue dots refer to the NPs. The radius and concentration of NPs are fixed at $R_P = 0.8R_g$ and $c_P = 0.02$, respectively.

Nanocomposites are put inside glass cells in experiments, which are modeled by hard walls, highlighted by brown color in Figure 1a for convenience. The interaction parameters between polymeric fluids and walls are set as zero (*i.e.*, the hard walls are assumed to be neutral).

In the parameter settings, the maximum Flory−Huggins interaction parameter of cylinder-forming diblock copolymers (*e.g.*, $f_A = 0.7$) is fixed at $(\chi_{AB}N)_{max} = 20.0$. The time step for eq 2 of local density fields is set as $\Delta t = 0.1\tau_C$, where the basic time unit is given by $\tau_C = \Delta x^2/M_K$ ($\Delta x$ is the discrete space in $x$ direction). In the case of NPs, the thickness of the interface has a value of $\lambda = 0.15R_g$. The interaction parameters between NPs and polymeric components are set as $(\chi_{AP}N)_{max} = 20.0$ and $\chi_{BP}N = 0$, corresponding to those in the case of B-like NPs. The mobility coefficient of NPs has a value of $M_P = 0.1M_K$. The time step of eqs 3 and 4 is $\Delta t_P = 0.01\tau_P$ as $\tau_P = \Delta x^2/M_P$. Under these parameter settings, the diblock copolymer/NP mixtures form a cylindrical phase with a periodicity $L_0$, which is in close relation with the concentration $c_P$ and radius $R_P$ of NPs (Figure S1 of the Supporting Information). To reduce computational costs for the inverse solution of $\varphi_M[\omega_M]$, the DSCFT/MD method is numerically executed in two-dimensional boxes with large sizes under a no-flux boundary condition in the $x$ direction and a periodic boundary condition in the $y$ direction. For a given concentration $c_P$ and radius $R_P$ of NPs, the dimensions of simulation boxes are set as $L_x \times L_y \approx 6\sqrt{3}L_0 \times 10.0L_0$, which are discretized by 320 × 320 grids. For the given parameter settings of zone-annealed nanocomposites, each DSCFT/MD simulation is repeated six times with different seeds of the random number generator. Details on how the integrated DSCFT/MD method is implemented for


https://dx.doi.org/10.1021/acs.macromol.1c00028
Macromolecules 2021, 54, 2561−2573

the nanocomposites with a spatiotemporal change of Flory−Huggins interaction parameters can be referred to in our previous works.[35,41,58]

**2.2. LSM of Micromechanics.** A Born LSM is utilized to capture micromechanical behaviors of highly heterogeneous materials, which are obtained from the output configurations of integrated DSCFT/MD simulations. The LSM has been applied to calculate micromechanical deformation of polymeric materials and has been shown to accurately recover their continuum elastic behaviors through appropriately choosing parameters of the computational model.[49−51] The LSM is composed of a network of harmonic springs connecting the nearest and next-nearest nodes. The elastic energy associated with the $o$-th node is expressed as

$$E_o = \frac{1}{2}\sum_q (\mathbf{u}_o - \mathbf{u}_q)^{\mathrm{T}}\cdot\mathbf{D}_{oq}\cdot(\mathbf{u}_o - \mathbf{u}_q) \tag{6}$$

where $\mathbf{u}_o$ is the displacement of the $o$-th node from its original position, and the summation is over all neighboring nodes. Herein, the symmetric matrix $\mathbf{D}_{oq}$ introduces elastic properties of the spring between the $o$-th and $q$-th nodes through the central force constant $k$ and non-central force constant $c$. For an isotropic medium (*e.g.*, pure diblock copolymers or NPs), Young's modulus $E$ and Poisson's ratio $\nu$ are related to the force constants *via* the following expressions in two dimensions, $E = 4k(k + c)/(3k + c)$ and $\nu = (k - c)/(3k + c)$. For the nanocomposites considered here, the local force constant $k_{o/q}$ at the $o$-th or $q$-th node is initially assigned in the startup of LSM simulations and strongly depends upon local density fields of different components. The force constants of springs are averaged from the connected nodes, that is, $k_{oq} = (k_o + k_q)/2$. In this work, the non-central force constant is set as zero to fix Poisson's ratio at $\nu \approx 0.33$.

The elastic force acting on the $o$-th node is a linear function of the local displacement of its neighboring nodes (*i.e.*, $\mathbf{F}_o = \sum_q \mathbf{D}_{oq}\cdot(\mathbf{u}_o - \mathbf{u}_q)$) due to the harmonic form of elastic energy in eq 6. As the spring constants are specified and external forces are applied to boundary nodes, nodal displacements are obtained through solving a set of sparse linear equations with the help of the conjugate gradient method. The local strain tensor $\boldsymbol{\varepsilon}$ can be calculated by a finite difference approximation of the displacement field, and the local stress tensor $\boldsymbol{\sigma}$ is obtained from the force acting on the nodes.[50] The scalar stress and strain values (*i.e.*, $\sigma_{xx}$ and $\varepsilon_{xx}$) correspond to the normal stress and strain components along the tensile direction, respectively. Finally, global Young's modulus $E$ of nanocomposites is calculated by dividing the applied stress by the average global strain.

## 3. RESULTS AND DISCUSSION

In this section, we first consider structural evolution of polymeric nanocomposites where the Flory−Huggins interaction parameters are spatially nonuniform but constant in time. In other words, stationary fronts of HZA are incorporated into the system of diblock copolymer/NP mixtures, which manifest epitaxial characteristics of structural evolution. Then, movable fronts are introduced to regulate the structural evolution of nanocomposites. The conditions that give rise to regularly well-ordered nanostructures of nanocomposites are pinpointed by the integrated DSCFT/MD simulations. Finally, outstanding mechanical properties of nanocomposites with regular arrays of NPs are demonstrated by the LSM calculations. We also briefly discuss the experimental realization for mechanically integrated multifunctional materials on the basis of the HZA method.

**3.1. Epitaxial Self-Assembly of Nanocomposites under Stationary Fronts.** Using the integrated DSCFT/MD method outlined above, we consider the structural evolution of nanocomposites subject to stationary fronts of HZA (*i.e.*, the moving speed $v$ is set as zero), which is schematically illustrated in Figure 1a. The solid line represents the profile of spatially localized Flory−Huggins interaction parameters $\chi_{AP}N = \chi_{AB}N$ (designated as $\chi N$ below). In all the simulations of HZA described herein, the minimum value $(\chi N)_{\min}$ within region III is set as 10.0, which is lower than the order−disorder transition value, $(\chi_{AB}N)_{ODT} \approx 14.0$, of pure diblock copolymers at $f_A = 0.7$. Since our simulations are performed in two dimensions, dot patterns of asymmetric diblock copolymers are akin to perpendicularly oriented cylinders.

To facilitate understanding about self-assembly behaviors of nanocomposites under such a spatially nonuniform field, we first probe into the responses of pure diblock copolymers to the same conditions. Figure 1b,c shows the density distribution of A-blocks and the three-dimensional height map at a late time, respectively. As expected, the asymmetric diblock copolymers within regions I and III produce B-rich cylindrical nanodomains (bright and green colors in Figure 1b,c) and remain in a disordered state, respectively. In particular, in region II, the appearance of a segregated pattern invades the featureless disordered phase. Our simulations for pure block copolymers well reproduce the earlier findings of numerical simulations of Ginzburg−Landau equations.[59−61]

In the next series of simulations, the invasion of the segregated pattern into the disordered phase is harnessed to guide the spatial arrangement and organization of NPs in a diblock copolymer matrix. We execute the DSCFT/MD simulations of polymeric nanocomposites subject to stationary fronts, where the B-like NPs are randomly distributed in region III of initial configurations. Figures 1d and S2 of the Supporting Information display the structural evolution of polymeric nanocomposites under a stationary field of Flory−Huggins interaction parameters. Unlike free dispersion of NPs in region III, a portion of B-like NPs migrate to the segregated pattern between cylindrical and disordered phases and accumulate in region II. Specifically, because of the responses of diblock copolymers to the spatially changed field, the intensity of the density field of A-blocks in region II is smaller than that in region I, but larger than that in region III, which is corroborated by Figure 1c. Such gradual A-rich domains near region II are able to exert a repulsion force on the B-like NPs due to their incompatibility, which drives a portion of B-wetted NPs to be located at the B-rich nanodomains within region II. As a result, the NPs could be directed to assemble into the ordered monolayer on the response layer of microphase-separated nanostructures of diblock copolymers in region II, which is highlighted by the arrow in Figure 1d.

From the conceptual framework of the atomic or molecular system, the crystallization process is generally analogous to the assembly of NPs widely regarded as "atom-equivalents".[62−64] From this point of view, assembling NPs onto the response layer of microphase-separated nanostructures of diblock copolymers has common ground with the epitaxial growth of atoms. In particular, when the interactions of NPs encapsulated in the cores of B-rich cylinders are weaker than those between


https://dx.doi.org/10.1021/acs.macromol.1c00028
Macromolecules 2021, 54, 2561−2573

encapsulated NPs and substrates (*e.g.*, the microphase-separated nanostructures considered here), the NPs are directed to assemble into flat monolayers in region II, termed as the "epitaxial assembly" process.[38,39] It is particularly noteworthy that excess NPs possibly further assemble onto the first layer of NP arrays after the NPs form a single layer (Figures 1d and S2 of the Supporting Information).

However, away from the response layer of diblock copolymers, as shown in Figures 1d and S2 of the Supporting Information, the distribution of NPs is still random, and the arrangement of NPs in a diblock copolymer matrix cannot achieve a higher regularity. We also perform additional simulations under different concentrations of NPs and minimum values $(\chi N)_{min}$ within region III. From Figures S2 and S3 of the Supporting Information, it is revealed that the epitaxial assembly of NPs only takes place near the response layer of microphase-separated nanostructures of diblock copolymers, resulting in a flat monolayer of NPs within region II. However, the diblock copolymers subject to stationary fronts cannot effectively program the epitaxial assembly of NPs into regularly well-ordered arrays in the entire simulation boxes. Below, we illustrate how to apply movable fronts to achieve well-ordered nanostructures that encompass both periodic ordering of cylindrical domains and regular arrays of NPs.

**3.2. Epitaxial Self-Assembly of Nanocomposites under Movable Fronts.** As demonstrated in our previous works,[35,36] by incorporating the movable fronts into the system of diblock copolymers without NPs, we could program the copolymer molecules to self-assemble into defect-free nanostructures in DSCFT simulations with larger boxes. Inspired by the intriguing findings, we examine the structural evolution and ordering kinetics of nanocomposites as the fronts of HZA are moved with a speed $v$ from the left to right sides of simulation boxes. The moving speed $v$ is denoted by the velocity unit $\tilde{v} = R_g/\tau_C$. The times are normalized by the quantity $T_v = L_x/v$, where $L_x$ is the box size in the $x$ direction. Given the box size $L_x = 6\sqrt{3}L_0 \approx 46.0R_g$ and the moving speed $v = 0.0075\tilde{v}$, movement of annealing fronts across the entire boxes takes roughly a time of $T_v \approx 6100.0\tau_C$.

Figure 2a shows the structural evolution of polymeric nanocomposites subject to movable fronts at speed $v = 0.0075\tilde{v}$. Initially, the Flory–Huggins interaction parameters in the entire system are set as $(\chi N)_{min} = 10.0$, and the NPs are randomly distributed in the homogenous state of diblock copolymers. Subsequently, the fronts are moved from the left to right sides of simulation boxes (as marked by yellow arrows). In the early stage (*e.g.*, $t = 0.1T_v$), the movable fronts direct the asymmetric diblock copolymers to form the first layer of B-rich cylinders encapsulating the NPs. In comparison with the spatial arrangement of NPs in the rest of the boxes, an important characteristic of these encapsulated NPs is that the individual NP is precisely placed into the core of a single B-rich cylinder. As the fronts keep continuously moving (*e.g.*, $t = 0.5T_v$), layers of cylindrical nanodomains sequentially appear in region II. The well-ordered cylinders act as structural scaffolds to host the B-like NPs and induce regular arrays of NPs. As the fronts are shifted to the right side of simulation boxes (*e.g.*, $t = 1.0T_v$), the diblock copolymers are programmed to self-assemble into hexagonal-packed defect-free cylinders, and the NPs are simultaneously directed to assemble into regularly well-ordered arrays.

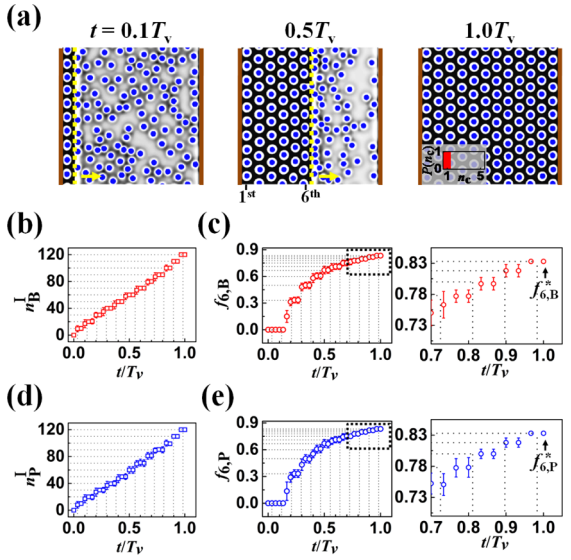


**Figure 2.** (a) Structural evolution of polymeric nanocomposites in the presence of movable fronts (highlighted by dashed lines) at speed $v = 0.0075\tilde{v}$. Insets show the weight distribution $P(n_c)$ of NPs' clusters within B-rich nanodomains. (b) Number $n_B^I$ of B-rich nanodomains within region I in terms of the time $t$. (c) Six-fold coordinated fraction $f_{6,B}$ of B-rich nanodomains in terms of the time $t$ and its zoomed image enclosed by the dashed box. (d) Temporal evolution of the number $n_P^I$ of NP clusters encapsulated by B-rich nanodomains. (e) Temporal evolution of six-fold coordinated fraction $f_{6,P}$ of NP clusters and its zoomed image. In panels (b–e), the dashed lines represent the predicted values of the geometric argument at the $w$-th layer. Each point is averaged over six independent runs, and the error bars stand for the standard deviations. The radius and concentration of NPs are fixed at $R_P = 0.8R_g$ and $c_P = 0.12$, respectively.

To evaluate the ordering kinetics of nanocomposites, we adopt the Delaunay triangulation to identify spatial arrangements of B-rich cylinders and NPs. Figure S4 of the Supporting Information illustrates a visual outline of the image analysis for the self-assembled nanostructures subject to movable fronts. Herein, the NPs are regarded as a cluster when the center distance of different NPs is smaller than $2.5R_P$. We only consider the B-rich nanodomains and NP clusters located in region I. The corresponding numbers are represented by $n_B^I$ and $n_P^I$, respectively. $n_{6,B}^I$ and $n_{6,P}^I$ stand for the numbers of six-fold coordinated B-rich nanodomains and NP clusters, respectively. The six-fold coordinated fraction $f_{6,B(P)}$ of B-rich nanodomains (NP clusters) is defined as $f_{6,B(P)} = n_{6,B(P)}^I/n_{B(P)}^I$. $f_{6,B(P)} \sim 1.0$ corresponds to the defect-free arrangement of B-rich nanodomains (NP clusters) in region I, while $f_{6,B(P)} \ll 1.0$ implies a defective arrangement. Noted that $f_{6,B(P)}$ has an upper limit value of $(n_L - 2)/n_L$ due to the non-periodic boundary condition in the $x$ direction, where $n_L$ is the total number of formed layers in the $x$ direction.

Figure 2b–e show the temporal evolution of the number $n_{B(P)}^I$ and six-fold coordinated fraction $f_{6,B(P)}$ of B-rich nanodomains (NP clusters) at speed $v = 0.0075\tilde{v}$. After incorporating movable fronts into the nanocomposites, a general feature in the temporal evolution of these quantities is sketched from these plots. These curves exhibit alternating plateaus and jump-ups, suggesting that the B-rich cylinders and the encapsulated NPs in region I are formed layer by layer. Furthermore, both the values of $f_{6,B}$ and $f_{6,P}$ approach the upper limit value of $(n_L - 2)/n_L$ as $n_L = 12$ at a late time. These


https://dx.doi.org/10.1021/acs.macromol.1c00028
Macromolecules 2021, 54, 2561–2573

observations manifest the fact that the polymeric nanocomposites subject to movable fronts have the capability to yield the self-assembled nanostructures with perfectly hexagonal-packed arrays of both cylinders and NPs.

To provide a definitive confirmation of the epitaxial self-assembly of nanocomposites, we propose a geometric argument to predict the number $n^{I}_{B(P)}$ and the six-fold coordinated fraction $f_{6,B(P)}$ of B-rich nanodomains (NP clusters) in the growth process of self-assembled nanostructures. As schematically illustrated in Figure S5 of the Supporting Information, $L_1$ and $L_{\|}$ represent the widths of the 1st layer and the $w$-th layer ($w = 2, ..., n_L - 1$), respectively. The time for the formation of the $w$-th layer is given by $t_w = (L_1 + L_{\|}(w - 1))/v$. At a time interval $t_{w-1} < t \leq t_w$, the number of B-rich nanodomains (NP clusters) is $n^{I}_{B(P)} = w \times (L_y/L_0)$. Correspondingly, the six-fold coordinated fraction is expressed as $f_{6,B(P)} = (w - 2)/w$ as $w \geq 2$. The dashed lines in Figure 2b–e highlight the predicted values of $n^{I}_{B(P)}$ and $f_{6,B(P)}$ at the $w$-th layer. The geometric argument well describes the growth process of self-assembled nanostructures as well as their arrangement, suggesting that the self-assembly of nanocomposites subject to HZA generally obeys the epitaxial process in the entire simulation boxes.

Furthermore, the spatial arrangement of NP clusters is measured by the weight distribution $P(n_c) = cn_c/n_P$, where $n_c$ means the number of clusters containing $c$ NPs within a B-rich nanodomain. As shown in the inset of Figure 2a, the weight distribution $P(n_c)$ of NP clusters has a value of one at $n_c = 1$, indicating that each B-rich nanodomain of diblock copolymers accommodates just one NP as the moving speed of fronts is low. Therefore, the phenomena observed from Figure 2 manifest the fact that an individual NP is precisely placed into each B-rich nanodomain, and eventually, the NPs are programmed to organize into regularly well-ordered arrays with the help of diblock copolymers subject to HZA.

The moving speed of fronts plays an important role in determining the self-assembled nanostructures and their ordering kinetics of polymeric nanocomposites. Figure 3a shows the structural evolution of nanocomposites subject to movable fronts at speed $v = 0.3000\tilde{v}$. As the movable fronts sweep across the entire simulation boxes, the asymmetric diblock copolymers eventually form defective cylinders, leading to poorly ordered arrays of NPs in the diblock copolymer matrix. Especially, multiple NPs are encapsulated into the B-rich nanodomains, which are demonstrated by the weight distribution $P(n_c)$ of NP clusters (inset of Figure 3a). Figure 3b–d shows the temporal evolution of the number $n^{I}_{B(P)}$ and six-fold coordinated fraction $f_{6,B(P)}$ of B-rich nanodomains (NPs' clusters). The values of $n^{I}_{B}$ and $n^{I}_{P}$ in the case of high speed deviate from the predicted values of the geometric argument highlighted by the dashed lines. Many defects like five- and seven-fold coordinated nanodomains are observed in the system, leading to smaller values of $f_{6,B}$ and $f_{6,P}$ in the self-assembly process of polymeric nanocomposites.

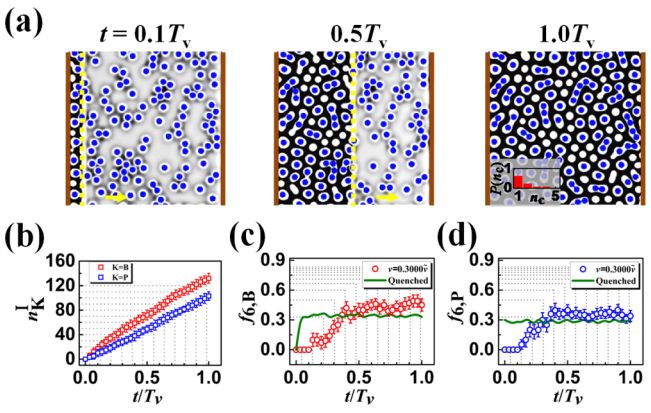


**Figure 3.** (a) Structural evolution of polymeric nanocomposites in the presence of movable fronts at speed $v = 0.3000\tilde{v}$. Inset shows the weight distribution $P(n_c)$ of NP clusters within B-rich nanodomains. (b) Numbers $n^{I}_{B}$ and $n^{I}_{P}$ of B-rich nanodomains and NP clusters in terms of the time $t$. (c) Six-fold coordinated fraction $f_{6,B}$ of B-rich nanodomains in terms of the time $t$. (d) Temporal evolution of six-fold coordinated fraction $f_{6,P}$ of NP clusters. The solid lines represent the case of quenched simulations of nanocomposites. In panels (b–d), the dashed lines represent the predicted values of the geometric argument.

It is helpful to compare the self-assembly behaviors of quenched and epitaxial nanocomposites. The quenched simulations of diblock copolymer/NP mixtures start from the homogenous state and instantaneously quench into the ordered state in entire simulation boxes (Figure S6 of the Supporting Information). Because the microphase separation of diblock copolymers is mainly triggered by the thermal fluctuations from different positions and directions, self-assembled nanostructures of quenched nanocomposites contain lots of arrested defects. By contrast, the microphase separation of epitaxial nanocomposites can also be triggered by the movable fronts within region II and propagate along the moving direction of the fronts. Consequently, in comparison with the results of quenched simulations (Figure S6 of the Supporting Information), the ordering degree of nanostructures is boosted by movable fronts *via* suppression of random instability. It should be mentioned that the ordering degree and formation pathway of nanostructures are strongly dependent upon the moving speed of the fronts. When the annealing fronts are moved slowly, thermal fluctuations inducing microphase separation are completely suppressed, and the annealing fronts direct the nanocomposites to epitaxially self-assemble into defect-free nanostructures (Figure 2). Under the circumstance of fast movement of annealing fronts, random instability of thermal fluctuations becomes effective, and long-lived defects finally remain in the self-assembled nanostructures (Figure 3), leading to slightly larger values of $f_{6,B}$ and $f_{6,P}$ in comparison with those of the quenched case.

In order to understand how the moving speed of annealing fronts impacts the epitaxial assembly of NPs in the diblock copolymer matrix, we consider microscopic details on trajectories of structural evolution (Figure 4) and motion of NPs in various regions (Figure 5). Figure 4 plots the three-dimensional height map of the density field $\varphi_A(\mathbf{r}, t)$ of A blocks at moving speeds $v = 0.3000\tilde{v}$ and $0.0075\tilde{v}$. For clarity, only a single NP is shown in the plots. As the annealing fronts are moved fast (Figure 4a), asymmetric diblock copolymers within the response layers produce metastable A- and B-rich flat layers (relative time $\Delta t = 0.03T_v$) because polymeric molecules do not have enough time to re-assemble themselves in region II.[35] Driven by the Brownian motion, NPs encapsulated by the AB diblock copolymers are entrapped by A-rich flat layers (inset of Figure 4a). As the annealing fronts continue to be moved, the encapsulated NPs enter into the B-rich flat layers ($\Delta t = 0.06T_v$), and subsequently, the B-like NPs guide the diblock copolymers to form B-rich cylinders. Consequently, strongly


https://dx.doi.org/10.1021/acs.macromol.1c00028
Macromolecules 2021, 54, 2561–2573

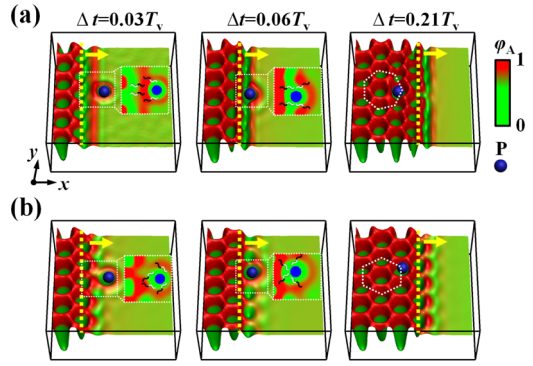


**Figure 4.** Three-dimensional height map of density field $\varphi_A(\mathbf{r}, t)$ of A blocks for moving speeds (a) $v = 0.3000\tilde{v}$ and (b) $v = 0.0075\tilde{v}$. Only a portion of the boxes is plotted. Insets show the zoomed images of the nanostructures enclosed by the dotted boxes and schematically illustrate the configurations of copolymer molecules. The dashed boxes in the right images highlight the lattice of B-rich nanodomains of diblock copolymers.

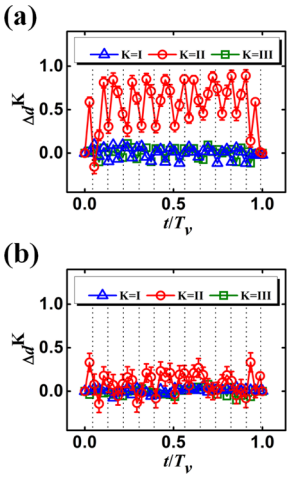


**Figure 5.** Effect of moving speed $v$ on the temporal evolution of the normalized position displacement $\Delta d^K$ of NPs in region K (K = I, II and III). (a) $v = 0.0075\tilde{v}$ and (b) $v = 0.3000\tilde{v}$. The regions I, II, and III are schematically illustrated in Figure 1a.

depending upon the position of unorganized B-like NPs, the B-rich cylinders of diblock copolymers may be arrayed into defective patterns with a poor arrangement of NPs ($\Delta t = 0.21T_v$).

When the annealing fronts are moved slowly (Figure 4b), the B-rich flat layers in region II are unstable and further transit into B-rich cylinders ($\Delta t = 0.03T_v$) because the diblock copolymer chains have enough time to re-assemble themselves in the response layers. A significant feature of these cylinders in region II is that they have a uniform size and identical position relative to that of the formed B-rich cylinders in region I, resulting from temporal evolution of metastable flat layers. Such cylinders are able to specifically collect B-like NPs in the response layers ($\Delta t = 0.06T_v$), originating from the compatibility between B blocks and NPs. That is, asymmetric diblock copolymers in the response layers direct the B-like NPs to epitaxially assemble at the fronts and form the organized monolayers. As the annealing fronts continue to move over the nanocomposites, the above scenarios are repeated, and the organized monolayers are iteratively produced at nearby fronts. As a result, the nanocomposites at low moving speed of fronts have the capability to epitaxially self-assemble into defect-free nanostructures with regular arrays of NPs ($\Delta t = 0.21T_v$).

Motion of NPs in the region K (K = I, II, and III) is characterized by the normalized position displacement $\Delta d^K = \sum_{i=1}^{n_p^K} \Delta \mathbf{d}_{i,x}/(n_p^K v \Delta T)$, where $\Delta \mathbf{d}_{i,x}$ represents the displacement of the $i$-th NP along the $x$ direction over a time interval (*e.g.*, $\Delta T = 0.0125T_v$) and $v\Delta T$ is the moving distance of annealing fronts. A large value of $\Delta d^K$ indicates a strong coupling between motion of NPs and movement of fronts. When $\Delta d^K$ approaches zero, the NPs display a weak coupling with the movable fronts.

Figure 5 depicts the effect of moving speed of annealing fronts on the temporal evolution of the normalized position displacement $\Delta d^K$ of NPs in region K. In region I, the B-like NPs are trapped into the B-rich nanodomains of microphase-separated diblock copolymers, resulting in a small value of $\Delta d^I$. In region III, the majority of NPs display a random motion in disordered fluids, leading to a small value of $\Delta d^{III}$. Thus, the moving speed of annealing fronts has a weak impact on the motion of NPs in regions I and III. However, a different scenario is observed for the effect of moving speed in region II. As the annealing fronts are moved slowly (*i.e.*, $v = 0.0075\tilde{v}$ in Figure 5a), a large value of $\Delta d^{II}$ implies the fact that the NPs are strongly coupled with the movement of the annealing fronts. In particular, the curve of $\Delta d^{II}$ exhibits periodic jump-ups and jump-downs in a reasonably well-defined time interval, originating from the fresh collection of NPs in the response layers and the final trap of NPs in the B-rich nanodomains. It should be mentioned that the time interval is about $T_v/(n_L - 1)$, which is approximately equal to the time interval of the monolayer formation. These features of NP motion further corroborate the formation of regular arrays of NPs layer by layer. However, for a high moving speed (*e.g.*, $v = 0.3000\tilde{v}$ in Figure 5b), the displacement of NPs in region II has a relatively small value, suggesting a weak coupling between motion of NPs and movement of fronts.

As illustrated above, the moving speed of annealing fronts has the capability to tune the formation pathway and the ordering degree of self-assembled nanostructures. Specifically, the epitaxial diblock copolymers subject to slow movable fronts direct the NPs nearby the response layers to assemble into regularly hexagonal-packed arrays (Figures 2, 4b, and 5a). When the moving speed of annealing fronts is increased, microphase separation of diblock copolymers is simultaneously triggered by the annealing fronts and the B-like NPs nearby the response layers, leading to poorly ordered arrays of NPs in the diblock copolymer matrix (Figures 3, 4a, and 5b).

The efficiency of the epitaxial self-assembly of polymeric nanocomposites subject to movable annealing fronts is evaluated by the final value $f_{6,B(P)}^*$ of the six-fold coordinated fraction of B-rich nanodomains (NP clusters), which is schematically represented in Figure 2. Figure 6a plots the final six-fold coordinated fraction $f_{6,K}^*$ (K = B and P) in terms of the moving speed $v$ of annealing fronts. As the fronts are moved slowly, there is sufficient time for the nanocomposites to self-assemble into well-ordered nanostructures. In particular, under the condition of $v \leq v^* = 0.0150\tilde{v}$, the movable fronts have the capability to realize the epitaxial growth of microphase-separated nanodomains of diblock copolymers, which serve as structural scaffolds to program the spatial arrangement of NPs in the diblock copolymer matrix. These characteristics of self-assembled nanostructures are identified


https://dx.doi.org/10.1021/acs.macromol.1c00028
Macromolecules 2021, 54, 2561−2573

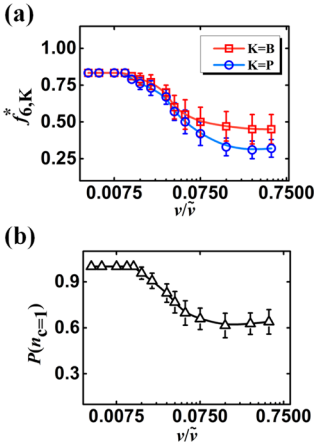


**Figure 6.** (a) Final six-fold coordinated fraction $f^*_{6,B(P)}$ of B-rich nanodomains (NP clusters) as a function of the moving speed $v$. (b) Weight distribution $P(n_c = 1)$ of a single NP in each B-rich nanodomain as a function of the moving speed $v$.

by large values of $f^*_{6,B}$ and $f^*_{6,P}$. When the fronts are moved fast, the diblock copolymer/NP mixtures form defective nanostructures filled by poor arrays of NPs, corresponding to a remarkable reduction of $f^*_{6,B}$ and $f^*_{6,P}$.

Two time scales $T_B$ and $T_P$ are introduced to estimate the critical speed $v^*$ of annealing fronts. $T_B$ is the time scale for the formation of cylinder monolayers or the movement of annealing fronts and is given by $T_B \approx L_\parallel/v = \sqrt{3}L_0/(2v) \approx 4\tau_C/(v/\tilde{v})$ at a typical value of $L_0 = 4.5R_g$. $T_P$ is the time scale of NP diffusion and can be roughly estimated as $T_P \equiv R_P^2/M_P \approx 284\tau_C$ as $R_P = 0.8R_g$. As $T_P < T_B$ (*i.e.*, the critical speed $v^* = 0.014\tilde{v}$), the diblock copolymers epitaxially self-assemble into well-ordered monolayers of cylinders, providing sufficient time to direct the organization of NPs into regular arrays (corresponding to the case of Figure 4b). The estimated value of $v^* = 0.014\tilde{v}$ is consistent with the findings of DSCFT/MD simulations (Figure 6).

Weight distribution $P(n_c = 1)$ of a single NP is used to characterize organization of NPs in the B-rich nanodomains. Figure 6b plots the weight distribution $P(n_c = 1)$ of a single NP as a function of the moving speed. In the case of low moving speed (*i.e.*, $v \leq 0.0150\tilde{v}$), an individual NP is placed in a single domain of B-rich cylinders. As the moving speed of annealing fronts is increased, the value of $P(n_c = 1)$ exhibits a remarkable decrease, implying that multiple NPs are positioned in the B-rich domains. In other words, precise organization of individual NPs into regular arrays cannot be realized by HZA with a high moving speed of annealing fronts.

It should be mentioned that the minimum value $(\chi N)_{min}$ within region III has a remarkable impact on the self-assembled nanostructures of polymeric nanocomposites subject to annealing fronts, which is demonstrated in Figure S7 of the Supporting Information. As the minimum value $(\chi N)_{min}$ is close to the order−disorder transition $(\chi N)_{ODT}$ of pure diblock copolymers (*i.e.*, corresponding to the case of CZA), the B-like NPs and the random fluctuations simultaneously induce microphase separation of block copolymers, leading to poor organization of NPs in the diblock copolymer matrix. When $(\chi N)_{min}$ is far below $(\chi N)_{ODT}$ (*i.e.*, corresponding to the case of HZA), the formation of self-assembled nanostructures is mediated by the annealing fronts, and the defect-free structures are finally achieved. Thus, in comparison with the results of CZA, the ordering degree of self-assembled structures of polymeric nanocomposites subject to HZA is remarkably boosted due to the emergence of epitaxial characteristics of diblock copolymers within region II.

In order to further validate the unique self-assembly behaviors of polymeric nanocomposites, we implement additional simulations for the hybrid systems of diblock copolymers with various compositions of A-blocks. As shown in Figure S8a of the Supporting Information, the B-like NPs dispersed in B-majority diblock copolymers (*e.g.*, $f_A = 0.3$) are directed to occupy the interstitial space within the hexagonally packed cylinders formed by A-minority blocks. In the case of $f_A = 0.5$, the nanocomposites display well-defined lamellae, with the NPs randomly hosted in B-rich nanodomains (Figure S8b of the Supporting Information), which are similar to the previous findings.[41]

We extend the box size of DSCFT/MD simulations for the large system of nanocomposites, which is shown in Figure S9 of the Supporting Information. With the help of movable fronts, the large system of nanocomposites finally forms the hexagonally packed defect-free patterns with regular arrays of NPs. Therefore, together with the findings of Figures 2−6, it is clearly revealed that the combination of diblock copolymers and HZA can be harnessed to kinetically manipulate both the ordering degree of self-assembled nanostructures of organic molecules and the spatial arrangement of inorganic NPs in the organic matrix through finely tuning the moving speed of the spatiotemporally dependent field.

**3.3. Effects of NP Concentration and Radius.** The concentration of NPs plays a significant role in programming the spatial arrangement and organization of NPs within the diblock copolymer matrix. To verify the outcome, the DSCFT/MD simulations are performed for fixing the radius $R_P$ of NPs while varying the concentration $c_P$ from 0.04 to 0.20. Figures 7 and S10 of the Supporting Information depict the effect of concentration $c_P$ of NPs on self-assembly behaviors of nanocomposites subject to movable fronts at speed $v = 0.0075\tilde{v}$. When the concentration $c_P$ of NPs is lower (*e.g.*, case of $c_P = 0.08$ in Figure 7a), the NPs are dominantly sequestered within B-rich domains in the left part of simulation boxes, arising from the sequential collection of NPs near movable fronts. By contrast, the right part of the simulation box contains B-rich cylinders of pure diblock copolymers due to depletion of NPs. Because of the incommensurability of periodicities of cylinders with and without NPs, the nanocomposites are guided to self-assemble into nanostructures consisting of long-lived defects, corresponding to a small value of $f^*_{6,B(P)}$. When the concentration of NPs is increased towards the optimum value $c_P^*$ at which a single NP is sequestered within each B-rich nanodomain, the nanocomposites are directed to self-organize into defect-free nanostructures with a precise organization of NPs (Figure 2), as evidenced by larger values of $f^*_{6,B(P)}$ and $P(n_c = 1)$. At a higher concentration of NPs (*e.g.*, case of $c_P = 0.14$ in Figure 7a), the annealing fronts have the capability to sequentially organize the NPs in the left part of simulation boxes. However, in the right part of simulation boxes, the remaining NPs hosted by the B-rich nanodomains become overcrowded, resulting in an increase of steric hindrance among neighboring NPs. As a result, the structural transition from hexagonally packed cylinders to lamellae is triggered by the swelling of B-rich nanodomains due to an increase of the NP loading in the right part of simulation boxes. Correspondingly, the B-rich nanodomains host multiple


https://dx.doi.org/10.1021/acs.macromol.1c00028
Macromolecules 2021, 54, 2561−2573

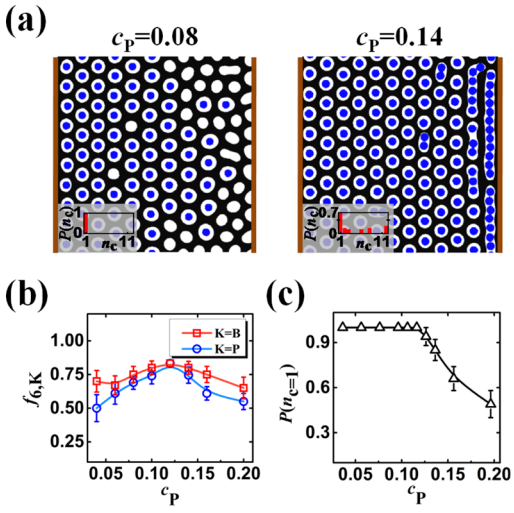


**Figure 7.** Effect of NP concentration $c_P$ on self-assembly behaviors of polymeric nanocomposites. (a) Self-assembled nanostructures of diblock copolymer/NP mixtures at the final stage of the epitaxial self-assembly under various concentrations of NPs. Inset shows the weight distribution $P(n_c)$ of NP clusters in each B-rich nanodomain. (b) Six-fold coordinated fraction $f^*_{6,B(P)}$ of B-rich nanodomains (NP clusters) in terms of the concentration $c_P$ of NPs. (c) Weight distribution $P(n_c = 1)$ of a single NP in each B-rich nanodomain in terms of the concentration $c_P$ of NPs. The moving speed of fronts and the radius of NPs are set as $v = 0.0075\tilde{v}$ and $R_P = 0.8R_g$, respectively.

NPs (case of $c_P = 0.14$ in the inset of Figure 7a). These phenomena result in reductions of $f^*_{6,B(P)}$ and $P(n_c = 1)$ as the concentration $c_P$ of NPs becomes high (Figure 7b,c).

As stated above, the hexagonal symmetry of self-assembled nanostructures of nanocomposites can be preserved with minimal or no defects, strongly depending upon the concentration of NPs. Using the geometrical argument, we can derive the optimum concentration $c_P^*$ of NPs for defect-free nanostructures to be $c_P^* = 2\pi R_P^2/\sqrt{3}L_0^2$, where $L_0$ is the periodicity of the NP-loaded hexagonal phase (Figure S1 of the Supporting Information). The argument predicts defect-free nanostructures occurring at $c_P^* = 0.115$ (for the radius $R_P = 0.8R_g$ of NPs and corresponding periodicity $L_0 \approx 4.5R_g$). The integrated DSCFT/MD simulations show a perfectly hexagonal symmetry of self-assembled nanostructures occurring at $c_P^* \approx 0.12$ (Figure 2). As shown in Figure 7b,c, the inclusion of NPs yields the well-ordered nanostructures as the concentration $c_P$ of NPs is selected to be near this optimum concentration $c_P^*$. It should be mentioned that the conditions for defect-free nanostructures only apply for the case of an individual NP within the core of the cylindrical nanodomain. In addition, for $c_P < c_P^*$, there are vacancy defects in the lattice of NP arrays, which are caused by an insufficient number of particles filling all of cylindrical nanodomains. Beyond the optimum concentration, cylindrical nanodomains tend to accommodate multiple particles instead of just one, distorting the symmetry of cylinder lattices.

Because of the increased swelling of self-assembled nanostructures of NP-loaded diblock copolymers, the radius $R_P$ of NPs impacts the self-assembly behaviors of nanocomposites subject to annealing fronts (Figure S11 of the Supporting Information). The DSCFT/MD simulations are performed for different radii of NPs ranging from $0.4R_g$ to $1.2R_g$, using an intermediate concentration $c_P = 0.12$ of NPs. Under the condition of $v = 0.0075\tilde{v}$, the pure diblock copolymers yield hexagonally packed cylinders without defects. Figure 8 shows the effect of NP size on the self-assembly

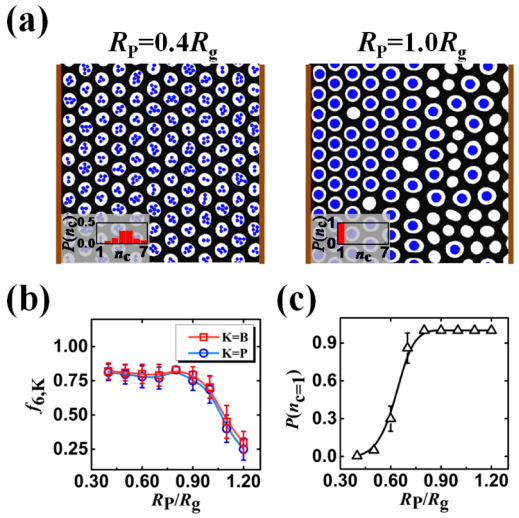


**Figure 8.** Effect of NP radius $R_P$ on self-assembly behaviors of polymeric nanocomposites. (a) Self-assembled nanostructures of nanocomposites at the final stage of the epitaxial self-assembly under various radii of NPs. The inset shows the weight distribution $P(n_c)$ of NP clusters in each B-rich nanodomain. (b) Six-fold coordinated fraction $f^*_{6,B(P)}$ of B-rich nanodomains (NP clusters) in terms of the radius $R_P$ of NPs. (c) Weight distribution $P(n_c = 1)$ of a single NP in terms of the radius $R_P$ of NPs. The concentration of NPs is set as $c_P = 0.12$.

behaviors of polymeric nanocomposites subject to movable fronts. For a fixed concentration of NPs, the number of smaller NPs (*e.g.*, $R_P = 0.4R_g$) becomes larger. The interiors of B-rich cylinders generally accommodate four or five NPs instead of just one, which is verified by the weight distribution $P(n_c)$. Although inter-particle repulsions give rise to a slight deformation of B-rich cylinders, the hexagonal symmetry of the entire lattice of nanostructures is maintained. These phenomena result in the regular arrays of NP clusters instead of individual NPs, corresponding to a larger value of $f^*_{6,B(P)}$ but a smaller value of $P(n_c = 1)$. At an intermediate radius of NPs (Figure 2), an individual NP is placed into the core of cylinders, and the arrangement of NPs is perfectly hexagonal, as reflected by larger values of both $f^*_{6,B(P)}$ and $P(n_c = 1)$. When the radius of NPs is further increased, corresponding to a decrease of the NP number, the shape and periodicity of B-rich cylinders in the left part of simulation boxes are remarkably affected by the encapsulated NPs. Because of the mismatch of lattice periodicities of B-rich cylinders with and without encapsulated particles, the nanocomposites finally form the defective nanostructures, as evidenced by a small value of $f^*_{6,B(P)}$. Thus, the intermediate radius of NPs gives better ordering due to encapsulation of individual NPs.

**3.4. Mechanical Properties of Nanocomposites.** We now turn our attention to characterize mechanical properties of nanocomposites subject to movable fronts. For this purpose, the self-assembled nanostructures obtained from the integrated DSCFT/MD simulations are directly fed into LSM calculations. In particular, the locations of different nanodomains of nanocomposites are mapped onto the grids of the LSM. It is assumed that both A and B components of diblock copolymers have same stiffness, but the NPs are 10 times stiffer than the


https://dx.doi.org/10.1021/acs.macromol.1c00028
Macromolecules 2021, 54, 2561−2573

polymeric matrix. The elastic properties of polymer/NP interfaces vary linearly with local density fields of NPs and diblock copolymers. In this way, we explore the effects of spatial arrangement and organization of NPs on mechanical properties of nanocomposites.

Using the LSM, we apply a stress along the moving direction of annealing fronts (*i.e.*, $x$ direction) at the boundaries and calculate the resultant normal stress field $\sigma_{xx}$ and strain field $\varepsilon_{xx}$ as well as global Young's modulus $E$ of nanocomposites. The relative quantities are defined as $(H - H_0)/H_0$, where $H = \sigma_{xx}$, $\varepsilon_{xx}$, or $E$ and $H_0$ is the corresponding responses of pure diblock copolymer materials. The contours of relative normal stress and strain fields are plotted in Figure 9a,b as well as Figures S12 and S13 of the Supporting Information. Some general observations are identified from these stress and strain plots. The stress concentrations within NPs can be seen as red regions, but the polymeric matrix surrounding NPs has relatively lower stress. Moreover, the strain values within NPs are significantly lower than those of the polymeric matrix due to a large disparity of elastic constants. The inability of stiff NPs to deform as the neighboring matrix results in strain concentrations along the tensile direction at the particle–polymer interfaces.

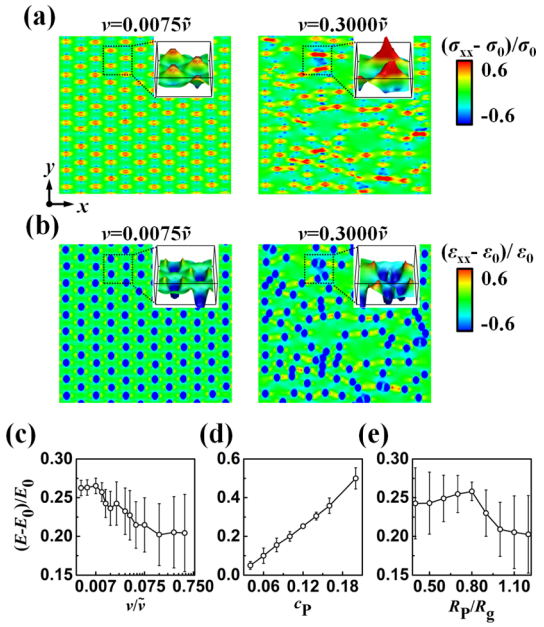


**Figure 9.** (a) Contour plots of the normal stress field $\sigma_{xx}$ for self-assembled nanostructures of polymeric nanocomposites subject to annealing fronts at speed $v = 0.0075\tilde{v}$ (see case of $t = 1.0T_v$ in Figure 2a) and $v = 0.3000\tilde{v}$ (see case of $t = 1.0T_v$ in Figure 3a). Insets illustrate the three-dimensional height map of the stress field enclosed by dashed boxes. (b) Contour plots of normal strain field $\varepsilon_{xx}$ and their zoomed images. (c–e) Global Young's modulus $E$ as a function of (c) the moving speed $v/\tilde{v}$ of annealing fronts, (d) concentration $c_P$, and (e) radius $R_P$ of NPs. Each data point is averaged over six calculations, and the error bars represent the standard deviations.

Beyond the general observations of contour plots of stress and strain fields, there exist some remarkable differences due to the incorporation of annealing fronts. As a representative example, Figure 9a,b shows the effect of the moving speed of annealing fronts on micromechanical properties of nanocomposites. One can deduce a significant outcome that the distributions of normal stress and strain fields are in close relation with the spatial regularity of NPs localized in the diblock copolymer matrix. In the case of moving speed $v = 0.0075\tilde{v}$, isolated and stiff NPs are regularly dispersed throughout the soft matrix of diblock copolymers, and the distance between neighboring NPs is larger, resulting in weaker stress and strain concentrations around NPs. As the moving speed is increased, the nanocomposites form defective nanostructures, and a portion of NPs produce clusters at the defects. From the contrast between the cases of $v = 0.0075\tilde{v}$ and $v = 0.3000\tilde{v}$ of Figure 9a,b, it is clear that intensities of stress and strain concentrations are significantly enhanced by the presence of defects. In particular, the stress concentrations are extended into the polymer matrix along the tensile direction and, in some cases, are overlapped. As a consequence, the system consisting of long-lived defects can form strands of stress concentrations in the tensile direction, which are highlighted in the inset of Figure 9a. This behavior is also apparent in the plots of the strain filed (Figure 9b). Stress and strain concentrations induced by defects are also observed in the nanocomposites with various radii and concentrations of NPs, which are respectively shown in Figures S12 and S13 of the Supporting Information. It should be pointed out that the stress and strain concentrations at the arrested defects are primarily responsible for the premature failure of entire materials.

By dividing the applied stress by the average global strain, we obtain global Young's modulus $E$ of nanocomposites and thereby gain an additional insight into the effect of the epitaxial assembly of NPs on mechanical properties of nanocomposites. Figure 9c–e depict relative Young's modulus of nanocomposites as a function of the moving speed $v/\tilde{v}$ of annealing fronts, the concentration $c_P$, and radius $R_P$ of NPs, respectively. As expected, the concentration of stiff NPs is the most important factor in determining the magnitude of Young's modulus (Figure 9d). As the NPs are programmed to epitaxially assemble into hexagonally packed arrays, the regular arrays of NPs dispersed in diblock copolymers are found to improve global stiffness of hybrid materials (Figure 9c,e). This is especially in the cases of low moving speed of annealing fronts and intermediate radius of NPs, where an individual NP is precisely localized in the core of an energetically favorable domain and entire structures display long-range ordering. Thus, the findings of Figure 9c,d provide some useful guidelines for rational design of functional materials with superiorly mechanical properties. Specifically, Young's modulus of polymeric nanocomposites can be effectively enhanced by adding more NPs into the hybrid materials. Meanwhile, the ordering degree of self-assembled nanostructures, which can be kinetically tuned by the processing of zone annealing, provides additional reinforcing elements to enhance strength of structural materials.

What is particularly noteworthy in Figure 9c–e is that the error bars standing for standard deviations dramatically decrease as the nanocomposites are programmed to self-assemble into well-ordered nanostructures. On the other hand, in the case of self-assembled nanostructures with lots of defects, these values of error bars remarkably increase, implying that the nanostructures and their mechanical properties are difficult to be accurately controlled. Thus, in order to obtain relatively excellent properties of functional materials, one has to eliminate the arrested defects of self-assembled nanostructures. The incorporation of movable fronts into the system of nanocomposites not only offers a


https://dx.doi.org/10.1021/acs.macromol.1c00028
Macromolecules 2021, 54, 2561–2573

novel strategy to accurately regulate the spatial organization of stiffer inorganic particles dispersed in a softer organic matrix but also provides an effective way for improving the stiffness of resultant materials.

We evaluate the effect of mesh sizes of LSM calculations and DSCFT/MD simulations on the mechanical properties of nanocomposites. As shown in Figure S14 of the Supporting Information, the change of mesh sizes of LSM calculations has a weak influence on the micromechanical behaviors of nanocomposites such as the distributions of stress fields and the stress transfer between neighboring NPs. The error bars of relative Young's modulus show a weak dependence upon the choice of the mesh size of DSCFT/MD simulations, which is depicted in Figure S15 of the Supporting Information.

It should be mentioned that the Born LSM presented here does not include the contributions of nonlinearity and anisotropy of real materials, especially the strong interactions between NPs and polymers. However, the phenomena of stress and strain concentrations in nanocomposites are more likely to occur as a consequence of the mismatch of elastic properties of polymers and NPs. Therefore, the findings of LSM calculations (*e.g.*, an increase of the ordering degree of NP arrays enhances the strength of polymeric nanocomposites) are representative of real systems of nanocomposites.

**3.5. Experimental Discussion.** The hybrid system demonstrated by our simulations can be realized in experimental research studies. Quickly developing methods, like thermal and laser zone annealing, give researchers an experimental toolbox in designing main elements for the system of zone-annealed nanocomposites. For instance, utilization of a hot wire heater in the equipment of zone annealing can generate a sharper thermal gradient field for production of perpendicularly oriented cylinders of diblock copolymer films.[31] More recently, with the advent of high-power laser sources, localized heating by a movable laser beam is gaining attention as an alternative of zone annealing to yield macroscopically aligned patterns of diblock copolymer films in several milliseconds.[65−67] Hence, given the tremendous progress in diversifying the technique of zone annealing and the significant advancement of synthetic strategies of inorganic NPs, all of the main elements for potentially realizing the system of zone-annealed nanocomposites are experimentally achievable.

From experimental perspectives, the theoretical results presented here will conceive a wide implication on the kinetic control over the spatial arrangement and organization of NPs dispersed in the polymers. Currently, there exist plenty of thermodynamic strategies for controlling the placement of functionalized NPs inside the polymeric matrix,[1] which have a tight relationship with the compatibility of NPs and their host polymers. Usually, the spatial arrangement and organization of NPs are not readily controlled by the thermodynamic approaches because the interaction-specified system is easy to be entrapped into the metastable configurations with lots of defects. In contrast, we propose a strategy of kinetically controlling the assembly pathway to build the regularly well-ordered arrays of NPs, which are constructed from the epitaxial self-assembly of polymeric nanocomposites in the course of zone annealing. It is theoretically demonstrated that the assembly pathway and motion of NPs inside the diblock copolymer matrix can be finely controlled by changing the moving speed of annealing fronts (Figures 4 and 5). Correspondingly, the spatial arrangement and organization of NPs are efficiently tuned by changing the moving speed of annealing fronts (Figures 2 and 3). Such a strategy of a kinetically controlled assembly pathway represents an important step toward precise organization of NPs into regular arrays with promising horizons for structural and optoelectronic applications.

Furthermore, by coupling the DSCFT/MD method for the polymeric nanocomposites with the LSM calculations for the micromechanics, we could interrelate the spatial organization of NPs and the macroscopic properties of nanocomposites. As shown in Figure 9, Young's modulus of nanocomposites is markedly boosted by the concentration of NPs. Meanwhile, the ordering degree of NP arrays provides additional reinforcing elements to enhance the strength of polymeric nanocomposites. These findings are corroborated by the experimental observations of polymeric nanocomposites.[47,48] In addition to the enhanced strength, the polymeric nanocomposites for optoelectronic applications should display the enhanced optical activity. We note that Tagliazucchi *et al.* have developed a theoretical model for the hybrid soft/plasmonic materials,[68] which can be used to calculate local density fields of grafted polymers and optical properties of polymer-modified NPs. In further studies, we will extend this model to examine the extremely enhanced resonances of optically active nanocomposites, which contain the periodically well-ordered arrays of plasmonic NPs.

## 4. CONCLUSIONS

In summary, the integrated DSCFT/MD method is extended to uncover the pivotal roles of zone-annealed diblock copolymers in the spatial arrangement and organization of NPs. It is found that the response layers of asymmetric diblock copolymers subject to HZA induce the epitaxial assembly of NPs, which results in the achievement of hexagonally packed well-ordered arrays with exactly one NP in the core of a polymeric nanodomain. Importantly, our simulations isolate the condition of the moving speed of annealing fronts to create the regularly well-ordered arrays of NPs, originating from the kinetically controlled assembly pathway. The spatial arrangement and organization of NPs also have a tight relationship with the concentration and radius of NPs. Furthermore, a micromechanical model is applied to examine the mechanical properties of polymeric nanocomposites. The ability to precisely organize the NPs into regular arrays can improve the mechanical performance of polymeric nanocomposites. We hope that our computational findings could stimulate synergic efforts of experimentalists and theorists to conceive the dynamic or driven self-assembly system of diblock copolymers as a design tool for precisely programing the spatial arrangement and organization of NPs.

## ■ ASSOCIATED CONTENT

### Supporting Information

The Supporting Information is available free of charge at https://pubs.acs.org/doi/10.1021/acs.macromol.1c00028.

Additional simulation results (PDF)

## ■ AUTHOR INFORMATION

### Corresponding Authors

**Liangshun Zhang** − *Shanghai Key Laboratory of Advanced Polymeric Materials, Key Laboratory for Ultrafine Materials of Ministry of Education, School of Materials Science and*



https://dx.doi.org/10.1021/acs.macromol.1c00028
*Macromolecules* 2021, 54, 2561−2573

*Engineering, East China University of Science and Technology, Shanghai 200237, China;* orcid.org/0000-0002-0182-7486; Email: zhangls@ecust.edu.cn

**Jiaping Lin** − *Shanghai Key Laboratory of Advanced Polymeric Materials, Key Laboratory for Ultrafine Materials of Ministry of Education, School of Materials Science and Engineering, East China University of Science and Technology, Shanghai 200237, China;* orcid.org/0000-0001-9633-4483; Email: jlin@ecust.edu.cn

### Authors

**Jiabin Gu** − *Shanghai Key Laboratory of Advanced Polymeric Materials, Key Laboratory for Ultrafine Materials of Ministry of Education, School of Materials Science and Engineering, East China University of Science and Technology, Shanghai 200237, China*

**Runrong Zhang** − *Shanghai Key Laboratory of Advanced Polymeric Materials, Key Laboratory for Ultrafine Materials of Ministry of Education, School of Materials Science and Engineering, East China University of Science and Technology, Shanghai 200237, China*

Complete contact information is available at: https://pubs.acs.org/10.1021/acs.macromol.1c00028

### Notes

The authors declare no competing financial interest.

## ■ ACKNOWLEDGMENTS

This work was supported by the National Natural Science Foundation of China (22073028, 21873029, and 51833003). We are grateful to Dr. G. A. Buxton of Robert Morris University for valuable help about calculations of the LSM.

## ■ REFERENCES

(1) Balazs, A. C.; Emrick, T.; Russell, T. P. Nanoparticle Polymer Composites: Where Two Small Worlds Meet. *Science* **2006**, *314*, 1107−1110.
(2) Grzelczak, M.; Vermant, J.; Furst, E. M.; Liz-Marzán, L. M. Directed Self-Assembly of Nanoparticles. *ACS Nano* **2010**, *4*, 3591−3605.
(3) Wu, Y.; Dong, N.; Fu, S.; Fowlkes, J. D.; Kondic, L.; Vincenti, M. A.; de Ceglia, D.; Rack, P. D. Directed Liquid Phase Assembly of Highly Ordered Metallic Nanoparticle Arrays. *ACS Appl. Mater. Interfaces* **2014**, *6*, 5835−5843.
(4) Zhang, H.; Cadusch, J.; Kinnear, C.; James, T.; Roberts, A.; Mulvaney, P. Direct Assembly of Large Area Nanoparticle Arrays. *ACS Nano* **2018**, *12*, 7529−7537.
(5) Xia, Y.; Whitesides, G. M. Soft Lithography. *Angew. Chem., Int. Ed.* **1998**, *37*, 550−575.
(6) Pileni, M.-P. Self-Assembly of Inorganic Nanocrystals: Fabrication and Collective Intrinsic Properties. *Acc. Chem. Res.* **2007**, *40*, 685−693.
(7) Nie, Z.; Petukhova, A.; Kumacheva, E. Properties and Emerging Applications of Self-Assembled Structures Made from Inorganic Nanoparticles. *Nat. Nanotechnol.* **2010**, *5*, 15−25.
(8) Ross, M. B.; Mirkin, C. A.; Schatz, G. C. Optical Properties of One-, Two-, and Three-Dimensional Arrays of Plasmonic Nanostructures. *J. Phys. Chem. C* **2016**, *120*, 816−830.
(9) Theiss, J.; Pavaskar, P.; Echternach, P. M.; Muller, R. E.; Cronin, S. B. Plasmonic Nanoparticle Arrays with Nanometer Separation for High-Performance SERS Substrates. *Nano Lett.* **2010**, *10*, 2749−2754.
(10) Hsu, S.-W.; Rodarte, A. L.; Som, M.; Arya, G.; Tao, A. R. Colloidal Plasmonic Nanocomposites: From Fabrication to Optical Function. *Chem. Rev.* **2018**, *118*, 3100−3120.
(11) Alivisatos, A. P.; Johnsson, K. P.; Peng, X.; Wilson, T. E.; Loweth, C. J.; Bruchez, M. P.; Schultz, P. G. Organization of 'Nanocrystal Molecules' using DNA. *Nature* **1996**, *382*, 609−611.
(12) Chiu, J. J.; Kim, B. J.; Kramer, E. J.; Pine, D. J. Control of Nanoparticle Location in Block Copolymers. *J. Am. Chem. Soc.* **2005**, *127*, 5036−5037.
(13) Tang, T.-Y.; Zhou, Y.; Arya, G. Interfacial Assembly of Tunable Anisotropic Nanoparticle Architectures. *ACS Nano* **2019**, *13*, 4111−4123.
(14) Leibler, L. Theory of Microphase Separation in Block Copolymers. *Macromolecules* **1980**, *13*, 1602−1617.
(15) Bates, F. S.; Fredrickson, G. H. Block Copolymer Thermodynamics: Theory and Experiment. *Annu. Rev. Phys. Chem.* **1990**, *41*, 525−557.
(16) Bates, F. S.; Hillmyer, M. A.; Lodge, T. P.; Bates, C. M.; Delaney, K. T.; Fredrickson, G. H. Multiblock Polymers: Panacea or Pandora's Box? *Science* **2012**, *336*, 434−440.
(17) Thompson, R. B.; Ginzburg, V. V.; Matsen, M. W.; Balazs, A. C. Predicting the Mesophases of Copolymer-Nanoparticle Composites. *Science* **2001**, *292*, 2469−2472.
(18) Zhao, Y.; Thorkelsson, K.; Mastroianni, A. J.; Schilling, T.; Luther, J. M.; Rancatore, B. J.; Matsunaga, K.; Jinnai, H.; Wu, Y.; Poulsen, D.; Fréchet, J. M. J.; Paul Alivisatos, A.; Xu, T. Small-Molecule-Directed Nanoparticle Assembly towards Stimuli-Responsive Nanocomposites. *Nat. Mater.* **2009**, *8*, 979−985.
(19) Raman, V.; Bose, A.; Olsen, B. D.; Hatton, T. A. Long-Range Ordering of Symmetric Block Copolymer Domains by Chaining of Superparamagnetic Nanoparticles in External Magnetic Fields. *Macromolecules* **2012**, *45*, 9373−9382.
(20) Nam, T. W.; Jeong, J. W.; Choi, M.-J.; Baek, K. M.; Kim, J. M.; Hur, Y. H.; Kim, Y.; Jung, Y. S. Single Nanoparticle Localization in the Perforated Lamellar Phase of Self-Assembled Block Copolymer Driven by Entropy Minimization. *Macromolecules* **2015**, *48*, 7938−7944.
(21) Chao, H.; Lindsay, B. J.; Riggleman, R. A. Field-Theoretic Simulations of the Distribution of Nanorods in Diblock Copolymer Thin Films. *J. Phys. Chem. B* **2017**, *121*, 11198−11209.
(22) Koski, J. P.; Ferrier, R. C.; Krook, N. M.; Chao, H.; Composto, R. J.; Frischknecht, A. L.; Riggleman, R. A. Comparison of Field-Theoretic Approaches in Predicting Polymer Nanocomposite Phase Behavior. *Macromolecules* **2017**, *50*, 8797−8809.
(23) Krook, N. M.; Ford, J.; Maréchal, M.; Rannou, P.; Meth, J. S.; Murray, C. B.; Composto, R. J. Alignment of Nanoplates in Lamellar Diblock Copolymer Domains and the Effect of Particle Volume Fraction on Phase Behavior. *ACS Macro Lett.* **2018**, *7*, 1400−1407.
(24) Ouk Kim, S.; Solak, H. H.; Stoykovich, M. P.; Ferrier, N. J.; de Pablo, J. J.; Nealey, P. F. Epitaxial Self-assembly of Block Copolymers on Lithographically Defined Nanopatterned Substrates. *Nature* **2003**, *424*, 411−414.
(25) Bita, I.; Yang, J. K. W.; Jung, Y. S.; Ross, C. A.; Thomas, E. L.; Berggren, K. K. Graphoepitaxy of Self-Assembled Block Copolymers on Two-Dimensional Periodic Patterned Templates. *Science* **2008**, *321*, 939−943.
(26) Kim, S. Y.; Nunns, A.; Gwyther, J.; Davis, R. L.; Manners, I.; Chaikin, P. M.; Register, R. A. Large-Area Nanosquare Arrays from Shear-Aligned Block Copolymer Thin Films. *Nano Lett.* **2014**, *14*, 5698−5705.
(27) Majewski, P. W.; Yager, K. G. Rapid Ordering of Block Copolymer Thin Films. *J. Phys.: Condens. Matter* **2016**, *28*, 403002.
(28) Tan, K. W.; Wiesner, U. Block Copolymer Self-Assembly Directed Hierarchically Structured Materials from Nonequilibrium Transient Laser Heating. *Macromolecules* **2019**, *52*, 395−409.
(29) Hashimoto, T.; Bodycomb, J.; Funaki, Y.; Kimishima, K. The Effect of Temperature Gradient on the Microdomain Orientation of Diblock Copolymers Undergoing an Order−Disorder Transition. *Macromolecules* **1999**, *32*, 952−954.
(30) Berry, B. C.; Bosse, A. W.; Douglas, J. F.; Jones, R. L.; Karim, A. Orientational Order in Block Copolymer Films Zone Annealed below

the Order−Disorder Transition Temperature. *Nano Lett.* **2007**, *7*, 2789−2794.
(31) Singh, G.; Yager, K. G.; Smilgies, D.-M.; Kulkarni, M. M.; Bucknall, D. G.; Karim, A. Tuning Molecular Relaxation for Vertical Orientation in Cylindrical Block Copolymer Films *via* Sharp Dynamic Zone Annealing. *Macromolecules* **2012**, *45*, 7107−7117.
(32) Mita, K.; Tanaka, H.; Saijo, K.; Takenaka, M.; Hashimoto, T. Ordering of Cylindrical Domains of Block Copolymers under Moving Temperature Gradient: Separation of ∇T-Induced Ordering from Surface-Induced Ordering. *Macromolecules* **2008**, *41*, 6787−6792.
(33) Angelescu, D. E.; Waller, J. H.; Adamson, D. H.; Register, R. A.; Chaikin, P. M. Enhanced Order of Block Copolymer Cylinders in Single-Layer Films Using a Sweeping Solidification Front. *Adv. Mater.* **2007**, *19*, 2687−2690.
(34) Zhang, H.; Zhang, J.; Yang, Y.; Zhou, X. Microphase Separation of Diblock Copolymer Induced by Directional Quenching. *J. Chem. Phys.* **1997**, *106*, 784−792.
(35) Cong, Z.; Zhang, L.; Wang, L.; Lin, J. Understanding the Ordering Mechanisms of Self-Assembled Nanostructures of Block Copolymers during Zone Annealing. *J. Chem. Phys.* **2016**, *144*, 114901.
(36) Wan, X.; Gao, T.; Zhang, L.; Lin, J. Ordering Kinetics of Lamella-Forming Block Copolymers under the Guidance of Various External Fields Studied by Dynamic Self-Consistent Field Theory. *Phys. Chem. Chem. Phys.* **2017**, *19*, 6707−6720.
(37) Hill, J. D.; Millett, P. C. Directed Self-Assembly in Diblock Copolymer Thin Films for Uniform Hemisphere Pattern Formation. *Macromolecules* **2019**, *52*, 9495−9503.
(38) Lovinger, A. J.; Chua, J. O.; Gryte, C. C. Studies on the $\alpha$ and $\beta$ forms of Isotactic Polypropylene by Crystallization in a Temperature Gradient. *J. Polym. Sci., Polym. Phys. Ed.* **1977**, *15*, 641−656.
(39) De Rosa, C.; Park, C.; Thomas, E. L.; Lotz, B. Microdomain Patterns from Directional Eutectic Solidification and Epitaxy. *Nature* **2000**, *405*, 433−437.
(40) Tang, C.; Wu, W.; Smilgies, D.-M.; Matyjaszewski, K.; Kowalewski, T. Robust Control of Microdomain Orientation in Thin Films of Block Copolymers by Zone Casting. *J. Am. Chem. Soc.* **2011**, *133*, 11802−11809.
(41) Gu, J.; Zhang, R.; Zhang, L.; Lin, J. Harnessing Zone Annealing to Program Directional Motion of Nanoparticles in Diblock Copolymers: Creating Periodically Well-Ordered Nanocomposites. *Macromolecules* **2020**, *53*, 2111−2122.
(42) Vaia, R. A.; Maguire, J. F. Polymer Nanocomposites with Prescribed Morphology: Going beyond Nanoparticle-Filled Polymers. *Chem. Mater.* **2007**, *19*, 2736−2751.
(43) Naskar, A. K.; Keum, J. K.; Boeman, R. G. Polymer Matrix Nanocomposites for Automotive Structural Components. *Nat. Nanotechnol.* **2016**, *11*, 1026−1030.
(44) Yanagioka, M.; Frank, C. W. Effect of Particle Distribution on Morphological and Mechanical Properties of Filled Hydrogel Composites. *Macromolecules* **2008**, *41*, 5441−5450.
(45) Maillard, D.; Kumar, S. K.; Fragneaud, B.; Kysar, J. W.; Rungta, A.; Benicewicz, B. C.; Deng, H.; Brinson, L. C.; Douglas, J. F. Mechanical Properties of Thin Glassy Polymer Films Filled with Spherical Polymer-Grafted Nanoparticles. *Nano Lett.* **2012**, *12*, 3909−3914.
(46) Cheng, S.; Bocharova, V.; Belianinov, A.; Xiong, S.; Kisliuk, A.; Somnath, S.; Holt, A. P.; Ovchinnikova, O. S.; Jesse, S.; Martin, H.; Etampawala, T.; Dadmun, M.; Sokolov, A. P. Unraveling the Mechanism of Nanoscale Mechanical Reinforcement in Glassy Polymer Nanocomposites. *Nano Lett.* **2016**, *16*, 3630−3637.
(47) Huang, Y.; Zheng, Y.; Sarkar, A.; Xu, Y.; Stefik, M.; Benicewicz, B. C. Matrix-Free Polymer Nanocomposite Thermoplastic Elastomers. *Macromolecules* **2017**, *50*, 4742−4753.
(48) Ondreas, F.; Lepcio, P.; Zboncak, M.; Zarybnicka, K.; Govaert, L. E.; Jancar, J. Effect of Nanoparticle Organization on Molecular Mobility and Mechanical Properties of Polymer Nanocomposites. *Macromolecules* **2019**, *52*, 6250−6259.
(49) Buxton, G. A.; Care, C. M.; Cleaver, D. J. A Lattice Spring Model of Heterogeneous Materials with Plasticity. *Modell. Simul. Mater. Sci. Eng.* **2001**, *9*, 485−497.
(50) Buxton, G. A.; Balazs, A. C. Lattice Spring Model of Filled Polymers and Nanocomposites. *J. Chem. Phys.* **2002**, *117*, 7649−7658.
(51) Buxton, G. A.; Balazs, A. C. Simulating the Morphology and Mechanical Properties of Filled Diblock Copolymers. *Phys. Rev. E: Stat., Nonlinear, Soft Matter Phys.* **2003**, *67*, 031802.
(52) Zhang, Q.; Gu, J.; Zhang, L.; Lin, J. Diverse Chiral Assemblies of Nanoparticles Directed by Achiral Block Copolymers *via* Nanochannel Confinement. *Nanoscale* **2019**, *11*, 474−484.
(53) Sides, S. W.; Kim, B. J.; Kramer, E. J.; Fredrickson, G. H. Hybrid Particle-Field Simulations of Polymer Nanocomposites. *Phys. Rev. Lett.* **2006**, *96*, 250601.
(54) Fredrickson, G. H. *The Equilibrium Theory of Inhomogeneous Polymers*; Oxford University Press: Oxford, 2006.
(55) Fraaije, J. G. E. M.; van Vlimmeren, B. A. C.; Maurits, N. M.; Postma, M.; Evers, O. A.; Hoffmann, C.; Altevogt, P.; Goldbeck-Wood, G. The Dynamic Mean-field Density Functional Method and its Application to the Mesoscopic Dynamics of Quenched Block Copolymer Melts. *J. Chem. Phys.* **1997**, *106*, 4260−4269.
(56) Nakayama, Y.; Kim, K.; Yamamoto, R. Simulating (Electro)-Hydrodynamic Effects in Colloidal Dispersions: Smoothed Profile Method. *Eur. Phys. J. E: Soft Matter Biol. Phys.* **2008**, *26*, 361−368.
(57) Hall, D. M.; Lookman, T.; Banerjee, S. Non-Equilibrium Particle-Field Simulations of Polymer-Nanocomposite Dynamics. *Chem. Eng. Sci.* **2009**, *64*, 4754−4757.
(58) Zhang, L.; Sevink, A.; Schmid, F. Hybrid Lattice Boltzmann/Dynamic Self-Consistent Field Simulations of Microphase Separation and Vesicle Formation in Block Copolymer Systems. *Macromolecules* **2011**, *44*, 9434−9447.
(59) Liu, F.; Goldenfeld, N. Dynamics of Phase Separation in Block Copolymer Melts. *Phys. Rev. A: At., Mol., Opt. Phys.* **1989**, *39*, 4805−4810.
(60) Paquette, G. C. Front Propagation in a Diblock Copolymer Melt. *Phys. Rev. A: At., Mol., Opt. Phys.* **1991**, *44*, 6577−6599.
(61) Chen, L.-Y.; Goldenfeld, N.; Oono, Y.; Paquette, G. Selection, Stability and Renormalization. *Phys. A* **1994**, *204*, 111−133.
(62) Zhuang, J.; Wu, H.; Yang, Y.; Cao, Y. C. Supercrystalline Colloidal Particles from Artificial Atoms. *J. Am. Chem. Soc.* **2007**, *129*, 14166−14167.
(63) Wang, M. X.; Seo, S. E.; Gabrys, P. A.; Fleischman, D.; Lee, B.; Kim, Y.; Atwater, H. A.; Macfarlane, R. J.; Mirkin, C. A. Epitaxy: Programmable Atom Equivalents Versus Atoms. *ACS Nano* **2017**, *11*, 180−185.
(64) Gabrys, P. A.; Zornberg, L. Z.; Macfarlane, R. J. Programmable Atom Equivalents: Atomic Crystallization as a Framework for Synthesizing Nanoparticle Superlattices. *Small* **2019**, *15*, 1805424.
(65) Jin, H. M.; Lee, S. H.; Kim, J. Y.; Son, S.-W.; Kim, B. H.; Lee, H. K.; Mun, J. H.; Cha, S. K.; Kim, J. S.; Nealey, P. F.; Lee, K. J.; Kim, S. O. Laser Writing Block Copolymer Self-Assembly on Graphene Light-Absorbing Layer. *ACS Nano* **2016**, *10*, 3435−3442.
(66) Jiang, J.; Jacobs, A. G.; Wenning, B.; Liedel, C.; Thompson, M. O.; Ober, C. K. Ultrafast Self-Assembly of Sub-10 nm Block Copolymer Nanostructures by Solvent-Free High-Temperature Laser Annealing. *ACS Appl. Mater. Interfaces* **2017**, *9*, 31317−31324.
(67) Leniart, A. A.; Pula, P.; Sitkiewicz, A.; Majewski, P. W. Macroscopic Alignment of Block Copolymers on Silicon Substrates by Laser Annealing. *ACS Nano* **2020**, *14*, 4805−4815.
(68) Tagliazucchi, M.; Blaber, M. G.; Schatz, G. C.; Weiss, E. A.; Szleifer, I. Optical Properties of Responsive Hybrid Au@Polymer Nanoparticles. *ACS Nano* **2012**, *6*, 8397−8406.


https://dx.doi.org/10.1021/acs.macromol.1c00028
*Macromolecules* 2021, 54, 2561−2573